

Transmission Electron Microscope Using a Linear AcceleratorTakumi Sannomiya^{1,2,*}, Yoshihiro Arai³, Kuniaki Nagayama^{4,5} and Yukinori Nagatani^{5,6,†}¹*Tokyo Institute of Technology, 4259 Nagatsuta, Midoriku, Yokohama, 226-8503 Japan*²*JST PRESTO, 4259 Nagatsuta, Midoriku, Yokohama, 226-8503 Japan*³*Terabase, Inc., 29-3 Arai, Myodaiji, Okazaki, Aichi, 444-0864 Japan*⁴*Life is Small. Company, 1-11-13-417 Minami-ota, Minamiku, Yokohama, 232-0006 Japan*⁵*National Institute for Physiological Sciences, 5-1 Higashiyama Okazaki, Aichi, 444-8787 Japan*⁶*KEK, High Energy Accelerator Research Organization, 4 Shirane Shirakata, Tokai-mura, Naka-gun, Ibaraki 319-1195 Japan*

(Received 7 May 2019; published 8 October 2019)

High-voltage transmission electron microscopes (HVTEMs), which can visualize internal structures of micron thick samples, intrinsically have large instrument sizes because of the static voltage isolation. In this Letter, we develop a compact HVTEM, employing a linear accelerator, a subpicosecond beam chopper, and a linear decelerator. 100 kV electrons initially accelerated by a static field are accelerated at radio frequency (rf) up to 500 kV, transmitting through the sample and finally rf decelerated down to 200 kV to be imaged through a 200 kV energy filter. 500 kV imaging, as well as subnanometer resolution at 200 kV, have been demonstrated.

DOI: [10.1103/PhysRevLett.123.150801](https://doi.org/10.1103/PhysRevLett.123.150801)

High-voltage transmission electron microscopes (HVTEMs) with an electron acceleration voltage higher than 300 kV have been used to achieve high spatial resolution based on the short wavelength of high-energy electrons, as well as to image thick samples taking advantage of the high transmissivity of electrons [1–3]. Since the advent of the aberration corrector, which enables atomic resolution even at low acceleration voltages [4–9], the role of high-voltage instruments has been directed more towards thick sample measurement, such as tomography for biological tissues or whole cells, *in situ* observation in a liquid or gas environment, and dislocation analysis of bulklike samples [10–12]. While HVTEMs still have the clear advantage of high transmissivity for thick samples, one of the serious drawbacks is the size of the instrumentation. A 1 MeV instrument typically requires a dedicated building due to the size of the electrical isolation of the static electric field for electron acceleration. In contrast, radio frequency (rf) accelerators even up to GeV are much more compact [13]. To realize a compact HVTEM, a combination with an rf linear accelerator (linac) had already been proposed in the 1970s [14–16]. The idea to use a high-frequency electromagnetic field in electron optics was also considered to correct the intrinsic aberrations of static round lenses [17]. More recently, time-resolved diffraction has been demonstrated using a rf cavity located at the electron source [18,19]. However, to date, no realistic microscope has been realized. The difficulty of the real space imaging mainly arises from the spatial and temporal coherence of the electron source, which is worsened by a poorly controlled rf field, as well as the Boersch effect when the electrons are accumulated in space.

After 50 years of unsuccessful history, we have here realized a linac transmission electron microscope (TEM) by adopting new technologies. In this Letter, we report its current performance. To overcome the coherence problem and to realize more compact HVTEM instrumentation, we introduced the following electron optics elements: (i) a subpicosecond beam chopper system with high spatial and temporal coherence, where the spatial motion and energy spread of the electron beam is canceled by two identical cavities; (ii) a decelerator placed right after the specimen to minimize the high-voltage electron path, which allows the utilization of the electron optics of a low-voltage instrument after the objective lens. The rf chopping is advantageous compared to pulsed photocathodes in order to synchronize the rf acceleration with accurate phase control and to minimize jitter.

The developed linac TEM instrument is based on a conventional 200 kV TEM (JEOL, 2200FS) with an omega-type in-column energy filter. An accelerator and a decelerator, as well as two electron beam chopper cavities (AET, Inc.), have been implemented in the TEM column. The objective lens has been replaced by a 500 kV compatible one. A schematic illustration of the whole microscope system is shown in Fig. 1. The electron beam is first statically accelerated to 100 kV in the 300 Hz-pulsed Schottky gun with a zirconia-coated tungsten emitter operated at 1800 K and then rf accelerated up to 500 kV to hit the specimen. Since the energy spread directly introduces the image blurring by the chromatic aberration of the objective lens (2.1 mm), the energy stability must be suppressed below 10^{-5} to achieve nanometer-scale spatial resolution. Considering the sinusoidal

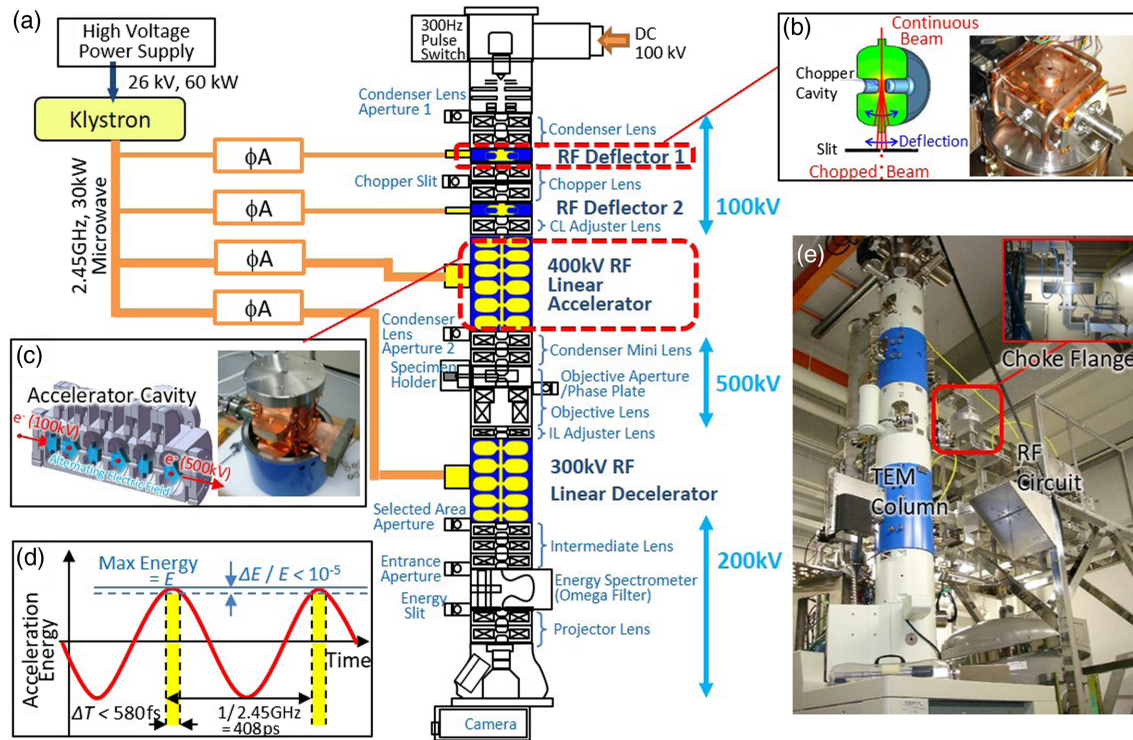


FIG. 1. Overview of the Linac-TEM. (a) Illustration of the whole system. CL and IL stand for condenser lens and intermediate lens, respectively. (b) Illustration and photograph of the rf deflector cavity. (c) Illustration and photograph of the accelerator cavity. (d) Schematic graph to show the acceleration condition. (e) Photograph of the whole instrumentation showing the TEM column (left) and rf waveguide circuit block (right). Choke flanges (inset) are used for the rf input of the acceleration and deceleration cavities in order to isolate the mechanical vibration.

modulation of the rf acceleration energy at 2.45 GHz, this stability limit corresponds to an energy window of 580 fs at the acceleration peak, as shown in Fig. 1(d) (see Supplemental Material for details of the acceleration [20]). After the objective lens, the electron beam with the specimen image information is decelerated by 300 kV down to 200 kV. The electron further travels through the omega-type energy filter to reach the camera screen. All the rf cavities are pumped to vacuum below 10^{-6} Pa to avoid discharges.

The 2.45 GHz microwave is supplied from a klystron (Toshiba Electron Tubes and Devices Co., Ltd.) with a maximum 30 kW power supply (IDX Co., Ltd.). The rf power is distributed to the two electron chopper cavities, acceleration cavity, and decelerator cavity, which are all water cooled. The rf power to the accelerator and decelerator cavities are input through the choke flanges [inset in Fig. 1(e)], which mechanically isolate the rf waveguide circuit and TEM column to avoid mechanical vibration. The rf phase and amplitude supplied to each cavity are controlled by the circulator and isolator in the rf circuit. The source frequency is controlled so that the accelerator cavity resonates and the resonance frequencies of the rest of the cavities are controlled by temperature.

The acceleration of the electron beam has been confirmed by measuring the electron wavelength using

diffraction patterns of a (001)-oriented Au single crystal, as shown in Fig. 2. The diffraction patterns were recorded by a screen inserted below the specimen [at the IL adjuster lens position in Fig. 1(a)] without exciting the lens between the sample and screen. Accelerated electron energy of 500 kV (400 kV rf acceleration from 100 kV) was confirmed at 8 kW input power to the acceleration cavity, as summarized in Fig. 2(b).

To realize the pulsed beam below 580 fs time width with high spatial and temporal coherence, we have developed a double-deflector chopping system that cancels the dynamic

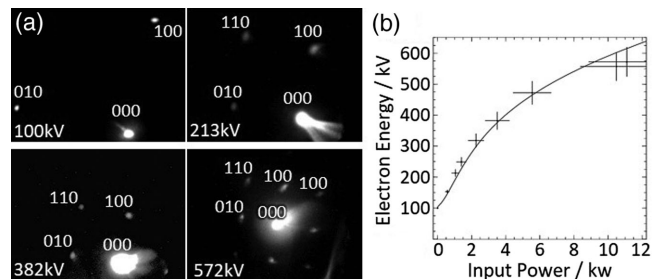


FIG. 2. Acceleration in the linac TEM. (a) Diffraction patterns of a (001)-oriented single-crystal Au sample at different acceleration voltages. (b) Acceleration plotted as a function of the input power in the acceleration cavity. The solid line shows the theoretically calculated acceleration voltage.

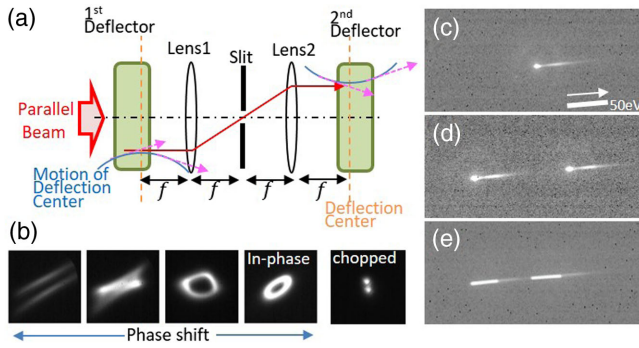


FIG. 3. Electron beam chopping. (a) Schematic illustration of the electron optics of the chopper system consisting of pairs of identical transfer lenses and beam deflecting rf cavities. (b) Observed electron beam traces on the slit plane at different relative phases of the two deflector cavities with the same input power. The slit-chopped image is shown in the rightmost image. (c)–(e) The spectral beam images on the energy plane using the energy filter (c) without chopping, (d) with chopping at 4 ps in the in phase condition, and (e) with chopping in the off phase condition by 1 mrad. The horizontal arrow direction corresponds to the energy loss. The spectra are obtained through a polycrystalline gold film. The images of (b)–(e) are recorded without rf acceleration.

motion of the beam, whereas a single beam deflector inevitably causes beam motion [21]. The newly developed chopper system consists of two rf deflector cavities that are optically superimposed by a lens pair in the $4-f$ configuration [Fig. 3]. The electron beam entering the first chopper cavity is deflected by a rf electric field and chopped by the slit located in the middle, as illustrated in Fig. 3(a). When the phase of the two deflector cavities are properly controlled, the deviation of the electron trajectory from the optical axis is canceled (see Supplemental Material [20]). To evaluate the beam motion, the beam trace on the optical plane corresponding to the slit position was monitored without acceleration [Fig. 3(b)]. In the out-of-phase condition [left images in Fig. 3(b)], the resultant beam trace is highly spread with a hyperbolic shape similar to a single rf deflector [22]. In the in phase condition, the beam trace converged to a small elliptic shape. Insertion of the slit in this condition results in two beam spots, corresponding to *forward* and *backward* traces with a relative phase difference of π between the two deflector cavity oscillations [rightmost images in Fig. 3(b)]. When the electron beam is accelerated by the rf accelerator, one of these two beams is totally out of phase and is filtered out by chromatic aberration of the lens or omega filter or is even reflected by the accelerator cavity. We also noticed that the energy spread due to the deflector cavity can be canceled by properly controlling the phase. This energy spread is due to the electric field utilized for deflection. Figures 3(c)–3(e) show the electron beam images with and without beam chopping on the energy-dispersive plane. The forward- and backward-chopped beams in Figs. 3(d) and 3(e) showed different energies gained from the deflector cavity. In the

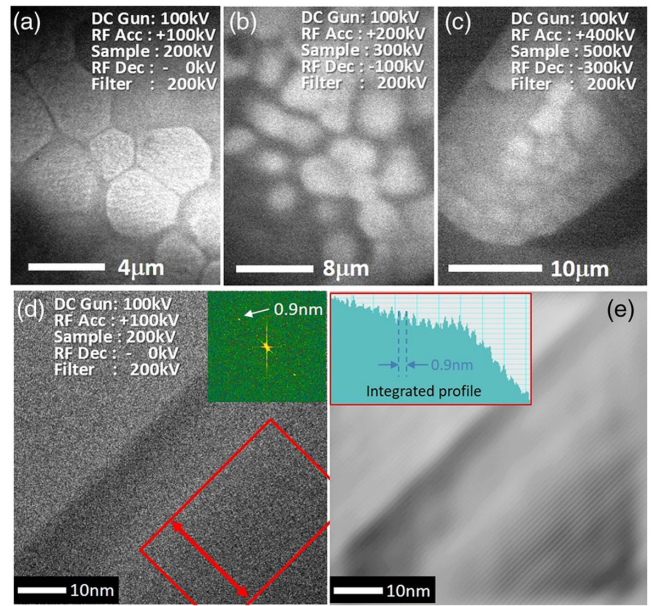


FIG. 4. Linac TEM Images. (a)–(c) Images of a Au film on a microgrid with acceleration and deceleration. (a) Image at 200 kV acceleration from the original 100 kV beam without deceleration (rf accelerated by 100 kV). (b) Image with a 300 kV electron beam at the sample position by 200 kV rf acceleration and detected at 200 kV by 100 kV deceleration. (c) Image with a 500 kV electron beam at the sample position by 400 kV rf acceleration and detected at 200 kV by 300 kV deceleration. All the images were acquired through the energy filter operated for 200 kV. (d),(e) Lattice imaging of a crocidolite sample obtained at 200 kV acceleration without deceleration. (d) Raw TEM Image. (Inset) Fourier transformed pattern showing 0.9 nm lattice fringe. (e) Fourier-filtered image using the 0.9 nm lattice spot. The lattice position at the right bottom is more clearly visible. The intensity profile integrated along the lattice direction of the raw data in (d) is shown in the inset. The profile is plotted along the red arrow direction in (d).

4-ps chopping condition with properly tuned phase and amplitude [Fig. 3(d)], the energy spread was identical to the original beam [Fig. 3(c)] [20], while a slightly misadjusted phase by 1 mrad resulted in ~ 30 eV energy spread [Fig. 3(e)]. The spectral images also show that the beam spread or split is only along the energy axis, meaning no spatial beam spread. These results confirm that a pulsed beam with high spatial and temporal coherence can be achieved by tuning the phase and amplitude of the chopper cavities. The phase of the rest of the cavities should also be tuned with respect to the phase of the chopped beam [see Fig. 1(a)].

Figure 4 shows the TEM images with rf acceleration and deceleration. The acceleration voltage was controlled from 100 to 400 kV, while the decelerator was operated in accordance with the accelerator so that the final beam energy is 200 kV. The final electron energy was confirmed by the energy filter with 200 kV setting. At the total acceleration energy of 200 kV with 100 kV rf acceleration,

the decelerator is turned off [Fig. 4(a)]. At 300 kV acceleration with 200 kV rf acceleration, the decelerator slows down the electron by 100 kV to achieve the final energy of 200 kV [Fig. 4(b)]. This demonstrates that electrons with the wave function carrying an image are decelerated by the rf decelerator and detected through electron optics systems with the image information maintained. Similar “image deceleration” had been reported for a camera system, however, by a static electric field and without lenses [23]. With acceleration up to 500 kV and deceleration by 300 kV, a TEM image was successfully acquired as shown in Fig. 4(c). The obtained images become blurred as the acceleration energy increases, which is due to the large energy spread as well as the spatial spread of the source. The scale of the smallest features in Figs. 4(b) and 4(c) with acceleration and deceleration is found to be around 500 nm, although this sample is not best suited for resolution check [20].

As the cause of image deterioration, we here note possible noise sources and solutions. (1) A small portion of the rf reflection backflew to the klystron and caused the unwanted oscillation of the signal. This noise could be suppressed by introducing additional isolators and strengthening the temperature feedback to keep the resonance condition. (2) Slight detuning of the phase of the decelerator can introduce a large energy spread even when the final average energy of the electron beam is kept constant to 200 kV. Better phase tuning can be realized by active and synchronized adjustment of the phase and amplitude by monitoring the energy spread or image blurring. (3) The environmental field can deviate the electron beam path, worsening the spatial coherence as well as temporal coherence due to the path change in the cavities. The cavities made of copper are the weakest position, as they are transparent against the external magnetic field, while lenses consist of magnetic materials automatically shielding the field. The klystron can also be disturbed by the external field. Such environmental noise can be reduced by better isolating the system or by introducing field cancellation coils. The reduction of these noise sources is planned for future improvement (see Supplemental Material for a more detailed evaluation of the noise, energy spread, and resolution [20]).

To see the resolution limit with rf acceleration, we tested the possibility of high-resolution lattice imaging. Figure 4(d) shows a raw TEM image of a crocidolite sample at 200 kV, where the original dc 100 kV beam is rf accelerated by 100 kV with the chopping pulse of 200 fs. At the right bottom of the image (indicated by red rectangle area), lattice fringes of 0.9 nm spacing along the fiber direction are captured, which can be more clearly seen as the spots in the FFT pattern in the inset. In the Fourier-filtered image [Fig. 4(e)], the position of the lattice can be confirmed. An integrated profile in the real space also shows a periodic intensity profile of the 0.9 nm lattice, as

shown in the inset. Although we could not achieve the theoretical limit of the resolution of 0.2 nm due to the above-mentioned energy spread, a subnanometer resolution has been proved at 200 kV with rf acceleration. We have also confirmed that the spatial resolution of 0.9 nm is well within the information transfer limit in this experimental condition (see Supplemental Material [20]).

In conclusion, we have developed a compact 500 kV TEM utilizing a linac system and experimentally demonstrated real space imaging in the nanoscale. To realize the linac TEM, we introduced a rf beam chopper, generating a subpicosecond electron beam pulse with high spatial and temporal coherence. The implemented linear decelerator allowed utilizing a conventional 200 kV TEM column with an energy filter, which slowed down the electrons with the image information maintained. At the acceleration voltage of 200 kV with 100 kV rf acceleration, the subnanometer lattice imaging was performed. These results prove the concept of a compact high-voltage linac TEM. Potentially, the acceleration of the linac TEM could be increased up to a few tens of MeV range, which becomes more realistic by employing superconducting magnetic lenses and cavities. Superconducting systems could reduce both size and energy consumption in the cavities [15]. To increase the electron number per pulse and to improve the energy resolution, a photocathode could be of use [24], provided that the rf synchronization is accurately controlled with properly chosen brightness considering the Boersch effect [25]. A terahertz linac system with a few-centimeter size might also be a possible future option [26,27]. We finally would like to remark on the similarity of this electron acceleration scheme to the electron energy gain technique recently used at optical frequencies, which offers electron beam manipulation by light [28,29].

This work was partly supported by JST-PRESTO JPMJPR17P8. The authors are thankful for the cooperation of all the individuals and companies involved in this work, especially, Dr. R. Aihara, Dr. T. Shirai, G. Ijima, Akimoto, JEOL, Inc., AET, Inc., IDX, Inc., ATA, Inc., Kashiwadenki, Inc., Dr. K. Murata, Dr. Y. Kayama, Z. Saito at NIPS, M. Ikeda, and Y. Kawaguchi at Terabase, Inc.

* sannomiya.t.aa@m.titech.ac.jp

† nagatani@nips.ac.jp

- [1] M. J. Makin and J. V. Sharp, *J. Mater. Sci.* **3**, 360 (1968).
- [2] J. M. Cowley, *J. Appl. Crystallogr.* **3**, 49 (1970).
- [3] R. F. Egerton, *Ultramicroscopy* **145**, 85 (2014).
- [4] M. Haider, S. Uhlemann, E. Schwan, H. Rose, B. Kabius, and K. Urban, *Nature (London)* **392**, 768 (1998).
- [5] O. L. Krivanek, P. D. Nellist, N. Dellby, M. F. Murfitt, and Z. Szilagy, *Ultramicroscopy* **96**, 229 (2003).
- [6] D. A. Muller, *Nat. Mater.* **8**, 263 (2009).
- [7] H. Sawada, T. Sasaki, F. Hosokawa, and K. Suenaga, *Phys. Rev. Lett.* **114**, 166102 (2015).

- [8] P. W. Hawkes, *Ultramicroscopy* **156**, A1 (2015).
- [9] M. Linck, P. Hartel, S. Uhlemann, F. Kahl, H. Muller, J. Zach, M. Haider, M. Niestadt, M. Bischoff, J. Biskupek, Z. Lee, T. Lehnert, F. Bornert, H. Rose, and U. Kaiser, *Phys. Rev. Lett.* **117**, 076101 (2016).
- [10] N. Tanaka, J. Usukura, M. Kusunoki, Y. Saito, K. Sasaki, T. Tanji, S. Muto, and S. Arai, *Microscopy* **62**, 205 (2013).
- [11] H. Mori, *J. Electron. Microsc.* **60**, S189 (2011).
- [12] K. Murata, S. Hagiwara, Y. Kimori, and Y. Kaneko, *Sci. Rep.* **6**, 34934 (2016).
- [13] A. Nassiri, B. Chase, P. Craievich, A. Fabris, H. Frischholz, J. Jacob, E. Jensen, M. Jensen, R. Kustom, and R. Pasquinelli, *IEEE Trans. Nucl. Sci.* **63**, 707 (2016).
- [14] M. Watanabe, T. Taoka, N. Anazawa, and S. Kato, *J. Phys. E: Sci. Instrum.* **7**, 412 (1974).
- [15] I. Dietrich, K. H. Herrmann, and C. Passow, *Optik (Stuttgart)* **42**, 439 (1975).
- [16] P. Hawkes and E. Kasper, *Principles of Electron Optics* (Academic Press, New York, 2017).
- [17] O. Scherzer, *Optik (Stuttgart)* **2**, 114 (1947).
- [18] Y. Muro'oka, N. Naruse, S. Sakakihara, M. Ishimaru, J. Yang, and K. Tanimura, *Appl. Phys. Lett.* **98**, 251903 (2011).
- [19] P. F. Zhu, Y. Zhu, Y. Hidaka, L. Wu, J. Cao, H. Berger, J. Geck, R. Kraus, S. Pjerov, Y. Shen, R. I. Tobey, J. P. Hill, and X. J. Wang, *New J. Phys.* **17**, 063004, (2015).
- [20] See Supplemental Material at <http://link.aps.org/supplemental/10.1103/PhysRevLett.123.150801> for details of the accelerator, beam chopper, energy spread, and contrast transfer function.
- [21] I. G. C. Weppelman, R. J. Moerland, J. P. Hoogenboom, and P. Kruit, *Ultramicroscopy* **184**, 8 (2018).
- [22] A. Lassise, P. H. A. Mutsaers, and O. J. Luiten, *Rev. Sci. Instrum.* **83**, 043705 (2012).
- [23] K. H. Downing and P. E. Mooney, *Rev. Sci. Instrum.* **79**, 043702 (2008).
- [24] A. H. Zewail, *Science* **328**, 187 (2010).
- [25] M. Kuwahara, Y. Nambo, K. Aoki, K. Sameshima, X. G. Jin, T. Ujihara, H. Asano, K. Saitoh, Y. Takeda, and N. Tanaka, *Appl. Phys. Lett.* **109**, 013108 (2016).
- [26] E. A. Nanni, W. Q. R. Huang, K. H. Hong, K. Ravi, A. Fallahi, G. Moriena, R. J. D. Miller, and F. X. Kartner, *Nat. Commun.* **6**, 8486 (2015).
- [27] D. F. Zhang, A. Fallahi, M. Hemmer, X. J. Wu, M. Fakhari, Y. Hua, H. Cankaya, A. L. Calendron, L. E. Zapata, N. H. Matlis, and F. X. Kartner, *Nat. Photonics* **12**, 336 (2018).
- [28] F. J. G. de Abajo and M. Kociak, *New J. Phys.* **10**, 073035 (2008).
- [29] B. Barwick, D. J. Flannigan, and A. H. Zewail, *Nature (London)* **462**, 902 (2009).